A sliced-3D approach to GPR FDTD modelling by optimising perfectly matched layers

Citation for published version:
Delf, R, Giannopoulos, A, Bingham, RG & Curtis, A 2021, 'A sliced-3D approach to GPR FDTD modelling by optimising perfectly matched layers', *Geophysics*, pp. 1-39. https://doi.org/10.1190/geo2020-0222.1

Digital Object Identifier (DOI):
10.1190/geo2020-0222.1

Link:
Link to publication record in Edinburgh Research Explorer

Document Version:
Peer reviewed version

Published In:
Geophysics

GEOPHYSICS®

A sliced-3D approach to GPR FDTD modelling by optimising perfectly matched layers

Journal:	*Geophysics*
Manuscript ID	GEO-2020-0222.R2
Manuscript Type:	Technical Paper
Keywords:	finite difference, electromagnetics, ground-penetrating radar (GPR), full-waveform inversion, boundary conditions
Manuscript Focus Area:	Electrical and Electromagnetic Methods, Ground-Penetrating Radar

A sliced-3D approach to GPR FDTD modelling by optimising perfectly matched layers

(April 29, 2021)

Running head: **Sliced-3d FDTD**

ABSTRACT

Finite-Difference Time-Domain (FDTD) forward modelling is often used to gain a more quantitative understanding of the interactions between electromagnetic fields and targets. To undertake full 3D simulations the computational demands are challenging, so simulations are often undertaken in 2D where assumptions in the propagation of electromagnetic fields and source type can result in errors. Here, we develop the concept of a sliced-3D simulation, wherein a thin slice of a 3D domain with strictly 2D geometry is used to minimise computational demands while obtaining synthetic waveforms that contain full 3D propagation effects. This approach requires optimisation of perfectly matched layer (PML) boundary condition parameters so as to minimise the errors associated with the source being located close to the boundary, and as a result of grazing-incident angle wave conversion to evanescent energy. We explore the frequency dependence of PML parameters, and establish a relationship between complex frequency stretching parameters and effective wavelength. The resultant parameter choice is shown to minimise propagation errors in the context of a simple radioglaciological model, where 3D domains may be prohibitively large, and for a near-surface cross-borehole survey configuration, a case where full waveform inversion may

typically be used.

INTRODUCTION

Finite-Difference Time-Domain (FDTD) forward modelling has been used in many areas of exploration and near-surface geophysics to test the performance of novel processing algorithms and acquisition (Versteeg, 1993; Langhammer et al., 2017), in data processing directly for finite difference and reverse time migration (Fisher et al., 1992; Yilmaz, 2001; Leuschen and Plumb, 2001; Church et al., 2018), and as a part of inversion algorithms including full waveform inversion (FWI) (Virieux and Operto, 2009; Busch et al., 2012; Mozaffari et al., 2016). In electromagnetic applications, 2D formulations of the Yee algorithm (Yee, 1966) are generally used, which make the implicit assumption of lateral model invariance. The resultant synthetic 2D data have an incorrect amplitude scaling with travel time for which a correction must be made. Many studies have employed a Bleistein filter (Bleistein, 1986; Auer et al., 2013) in pre-processing of field data to enable comparison with 2D models (Mozaffari et al., 2016; Klotzsche et al., 2019), but it has been demonstrated that this can result in errors after the first break or in complex velocity models (Auer et al., 2013).

Reduction to 2D requires the operator to assume that the radar antennas are either cross-line or in-line, modes that are typically and hereafter denoted TMz and TEz respectively. The most commonly-used modelling platforms apply TMz reduction from the principle that cross-line antennas are more widely used in many fields. However, the importance of source polarisation has been noted in several areas of the literature, including in glaciology (Langhammer et al., 2017), where the TEz mode is more commonly applied in ground-based studies (e.g., Bingham et al. (2017)). To address the issues outlined above, 3D modelling must be developed, yet the computational demands are intense, and therefore there is a need to develop a computationally efficient approach to modelling 3D fields.

In this paper, we seek to minimise the computational cost of full ~~polarisation~~ FDTD modelling of 2D geometries using a sliced-3D approach in gprMax, an open-source GPR modelling package (Warren et al., 2016). To do so we must optimise the boundary conditions, implemented by perfectly matched layers (PMLs) so as to attenuate noise due to grazing-wave interactions with the model boundaries. We investigate the frequency dependence of PML performance for the sliced-3D application, and demonstrate the effectiveness of the approach by applying the technique to two synthetic case studies where full 3D models can be prohibitively large and where assumptions about the source and propagation mechanisms, that are implicit in 2D modelling, do not hold.

THEORETICAL BACKGROUND

Approaches to modelling 2D geometries

FDTD modelling is generally undertaken using Yee's algorithm (Yee, 1966; Taflove and Hagness, 2005). In brief, the algorithm involves a discretisation of Maxwell's equations of electrodynamics, and an iterative propagation of a source term through time steps. The algorithm can be implemented in 3D or simplified to 2D in the TMz mode by assuming an infinitely long z-polarized dipole antenna (i.e. a line source) and cross-line geometry invariance to remove invariant E and H field components (Taflove and Hagness, 2005) (Figure 1). 2D simulations comprise a computationally quick method of modelling the response of a laterally invariant model. In practice, however, the assumption of an infinite z-polarised source is often violated due to the field logistics imposed on many GPR surveys.

For example, due to the low frequencies often used in ground-based glaciological radio-echo sounding (Scott et al., 2010; Sevestre et al., 2015; King et al., 2016), lengthy dipole antennas are often towed in-line to the survey direction and as such cannot be modelled accurately using 2D FDTD algorithms.

Additional issues with the 2D approach are encountered in the scaling of amplitude with travel time. In a 3D domain with a point source, $A \propto \frac{1}{r}$, where A is amplitude and r is distance, but in 2D the source becomes an infinite dipole and the relationship becomes $A \propto \frac{1}{\sqrt{r}}$ (Bleistein, 1986; Auer et al., 2013). Because of this, when 2D modelling is employed the results need to be post-processed to obtain amplitudes that quantitatively match field data. The 2D Green's function can be transformed between 2D and an equivalent 3D function through a $\frac{\pi}{4}$ phase shift and an amplitude scaling using the Bleistein filter (Bleistein, 1986), expressed in the frequency domain as

$$G^{3D}(\omega) = G^{2D}(\omega)\sqrt{\frac{|\omega|}{2\pi\sigma}}\exp\Big(-\operatorname{sgn}(\omega)\frac{j\pi}{4}\Big) \tag{1}$$

where G^{2D} and G^{3D} are the 2D and 3D Green's functions, ω is angular frequency, $j = \sqrt{-1}$ and $\operatorname{sgn}(\omega)$ is the signum function of ω. σ is a scaling factor $\sigma = cr$, where r is distance (m) and c is velocity of propagation (ms^{-1}). This widely-used function (e.g. Deregowski and Brown, 1983; Vidale et al., 1985; Esmersoy and Oristaglio, 1988; Yang et al., 2013; Lomas and Curtis, 2019) is an asymptotic solution making the far-field assumption that distance $r \gg \lambda$, the wavelength of the signal, hence the near-field phase corrections are incorrect. The scaling function σ is commonly estimated for the first break arrival and is often inaccurate for the cases of (a) heterogeneous media, where c and r are uncertain or complex, and (b) for later arrivals after the first break. Inaccurate amplitudes result in a degraded performance for FWI algorithms (Auer et al., 2013), resulting in more complex approaches requiring a good starting velocity model to be used (Van Vorst et al., 2014).

To overcome issues of amplitude scaling, and to retrieve EM polarisations in the in-line survey orientation using a 2D modelling domain, several authors have used 2.5D implementations of the Yee algorithm. These project the 3D algorithm onto a 2D plane by iterating over a series of constant wavenumbers k_z (e.g. Stoyer and Greenfield, 1976; Moghaddam et al., 1991; Xu and McMechan, 1997). This approach involves multiple easily parallelisable 2D syntheses, yet requires a reformulation of the Yee algorithm and post-processing of results, meaning that they have not, to date, been readily implemented in open-access FDTD software packages.

Sliced-3D FDTD modelling

While the above approaches to data pre-processing are effective in converting processing to a 2D problem, full 3D FDTD modelling of 2D geometries remains the optimal solution for generating full 3D polarisation and propagation effects (e.g. Mozaffari et al., 2016; Langhammer et al., 2017), although the computational demands of this approach can be significant. Minimising the width of a 3D domain is therefore desirable to minimise computational requirements, while retaining the benefits of 3D modelling. This we refer to as a sliced-3D approach, as it uses the 3D FDTD algorithm with a laterally-invariant 2D geometry, hence retaining the aforementioned correct amplitude scaling and source polarization capabilities. In the following we show that minimising the domain width can only be achieved through optimisation of boundary conditions, and that a such a sliced-3D approach can show improvements over 2D modelling for near-surface GPR modelling.

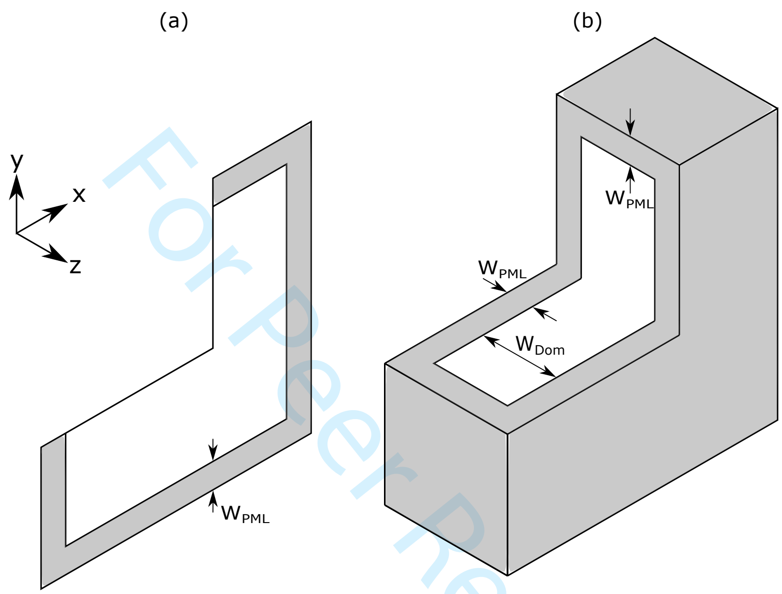

Figure 1: Schematic of (a) a 2D model and (b) a sliced-3D model, where $W_{Dom} > dx$; $W_{PML} = 15$ for both cases. Grey represents the PML region and white represents the model domain. The 2D model uses a 2D FDTD grid, while the sliced-3D model is a 3D FDTD domain with a minimised z domain width, bounded on all sides by a CFS-PML.

Perfectly Matched Layers

The boundaries of an FDTD grid are often terminated using a perfectly matched layer (PML) in which a complex stretching function s_u is used to both scale the model domain, and provide a mechanism for reflectionless signal attenuation. In the PML region, using cyclic notation $(i, j, k) \in (x, y, z), (y, z, x), (z, x, y)$ (Giannopoulos, 2018), Maxwell's equations become

$$j\omega \tilde{D}_i = \frac{1}{s_j}\frac{\partial \tilde{H}_k}{\partial j} - \frac{1}{s_k}\frac{\partial \tilde{H}_j}{\partial z} \tag{2}$$

$$j\omega \tilde{B}_i = \frac{1}{s_k}\frac{\partial \tilde{E}_j}{\partial k} - \frac{1}{s_j}\frac{\partial \tilde{E}_k}{\partial j} \tag{3}$$

Minimising the z-dimension of a 3D model results in energy propagating within the model domain at grazing (low-incidence) angles to the PML boundary, hence we use a complex frequency stretched PML (hereafter, CFS-PML) (Roden and Gedney, 2000; Berenger, 2002; Taflove and Hagness, 2005; Giannopoulos, 2008) where the stretching function s_u is of the form,

$$s_u = \kappa_u + \frac{\sigma_u}{\alpha_u + j\omega\epsilon_0}, \tag{4}$$

where $u \in (i, j, k)$ is the orientation perpendicular to the model boundary, κ_u is a unitless quantity which dictates a real coordinate stretch in the PML region, α is a frequency shift factor, and $\frac{\sigma}{j\omega}$ introduces an imaginary spatial coordinate stretch mainly responsible for signal attenuation. In this paper we assume that the PML parameters are the same in each orientation, so we will refer to s_u, α_u, κ_u and σ_u as s, α, κ and σ, respectively.

The CFS-PML parameters can be tuned to improve performance over a frequency range and reduce non-physical reflections from the PML boundary. This is done by scaling parameters α, κ and σ through the PML, usually using an integer polynomial m. σ is scaled

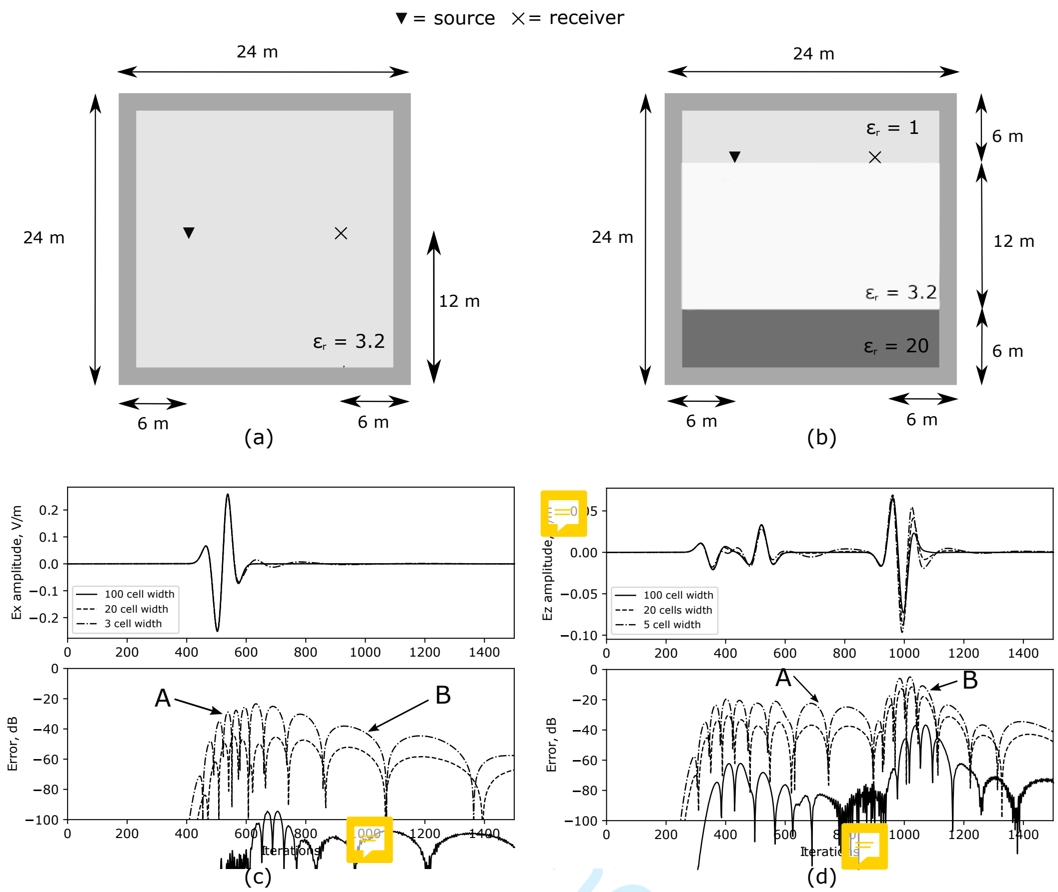

Figure 2: Comparison of the effects of cross-line domain size (in/out of the page), for (a and c) a homogeneous ice ($\epsilon = 3.2$) model with a Gaussian wavelet and a standard PML, and (b and d) a 3-layer model with a homogeneous ice layer overlying flat bedrock with a free-space layer above the surface. $dx = 0.1m$ and PMLs are 10 cells thickness. Two sources of noise can be noted for each; 'A' shows high frequency noise as a result of normal incidence reflections through the PML. The arrival time of this noise is delayed in wider implementations, as the two way travel time between boundaries (out of the plane in (a) and (b)) increases. 'B' shows low-frequency, evanescent noise as a result of grazing wave interactions between the signal and PML boundary. A wider model results in minimisation of this noise, as the incidence angle increases with increasing width.

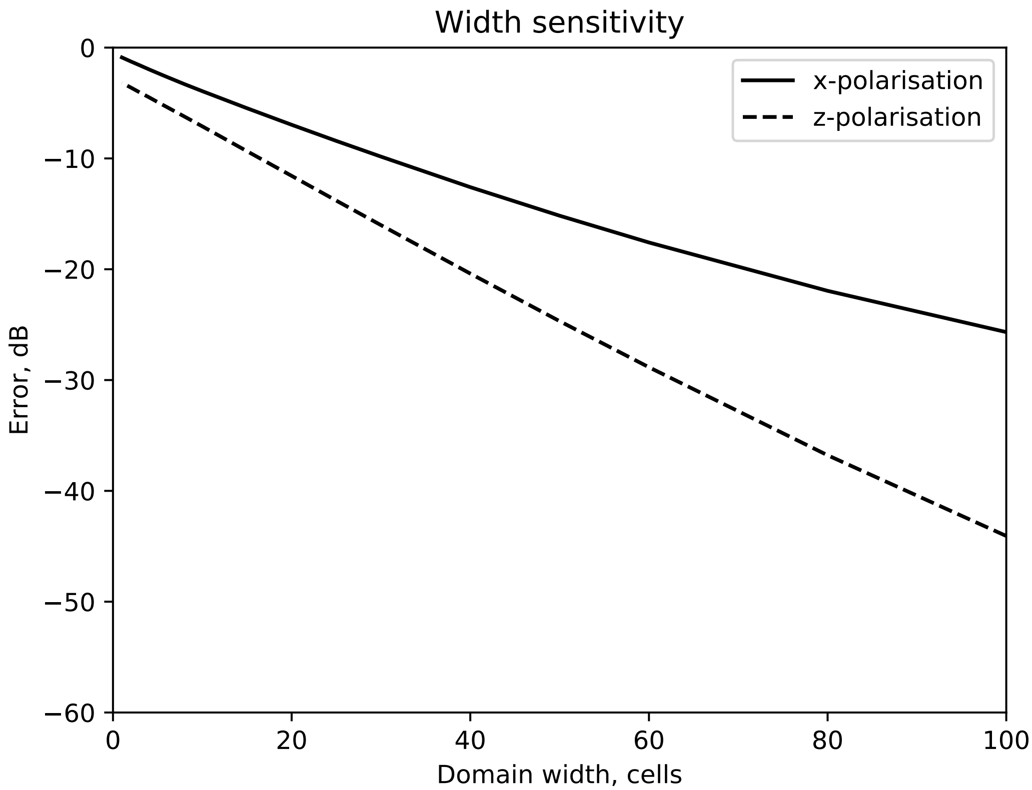

Figure 3: Plot of maximum error as a function of domain width for a homogeneous ice model shown in Figure 2(a). Decreasing model width results in an increased error as a result of interactions with grazing-angle incident energy.

from 0 to σ_{max} as

$$\sigma(x) = \sigma_{max}\left(\frac{x}{d}\right)^{m}, \tag{5}$$

where d is the depth of the PML in cells and $0 < x < d$ is the location within the PML so as to avoid sudden changes in σ and associated non-physical reflections. We use the commonly-used (Gedney and Zhao, 2010; Giannopoulos, 2012) estimate of optimum σ_{max}

after Gedney (1996) whereby

$$\sigma_{max} \approx \frac{m+1}{150\pi dx\sqrt{\epsilon_r}}, \tag{6}$$

where m is a polynomial scaling, dx is the spatial resolution, and ϵ_r is the relative dielectric constant. κ is similarly often scaled from 1 to κ_{max} by

$$\kappa(x) = 1 + (\kappa_{max} - 1)\Big(\frac{d-x}{d}\Big)^m, \tag{7}$$

such that $\kappa = 1$ (no coordinate stretch) at the model/PML interface and $\kappa = \kappa_{max}$ at the grid boundary.

The frequency shift factor α is generally scaled from a maximum at the model/PML boundary to zero at the outermost grid boundary, to minimise the reflection coefficient at the PML/model boundary (Taflove and Hagness, 2005) and provide broadband attenuation within the PML. Hence,

$$\alpha(x) = \alpha_{max}\Big(\frac{1-x}{d}\Big)^m \tag{8}$$

Higher order CFS-PMLs operate via a product of multiple contributions, by

$$s = \prod_{i=1}^{N} s_i \tag{9}$$

where N is the number of terms, i is the order, and s_i is defined in equation (4), with the aim of combining the characteristics of improved attenuation within the PML compared to the standard PML with the attenuation of evanescent energy of the CFS-PML. Typically, two terms ($N = 2$ in equation 9) are used for a higher order PML, but more terms are possible by introducing further terms of s_i. Feng et al. (2017) undertook an optimisation of the higher order PML for the application of broadband seismic modelling and showed a reduction in the error as a result. However, it is clear from inspection that such implementations introduce cross-terms in addition to the desired terms as, for a 2nd order CFS-PML

$$s = \left(\kappa_1 + \frac{\sigma_1}{\alpha_1 + j\omega\epsilon_0}\right)\left(\kappa_2 + \frac{\sigma_2}{\alpha_2 + j\omega\epsilon_0}\right) \tag{10}$$

~~(Giannopoulos, 2018).~~ What remains unclear is what impact these additional cross-terms have in an optimisation process. Along with the higher number of degrees of freedom associated with multiple stretching functions, this results in the process becoming a cumbersome problem for the general case, and hence will not be considered in this study.

METHODOLOGY

We initially demonstrate the impact of using a small cross-line domain size on signal error as a result of the aforementioned evanescent energy. We demonstrate the effect of reducing the cross-line domain size for both a homogeneous ice ($\epsilon_r = 3.2$) model (Figure 2a), and a layered model of homogeneous ice overlying a bedrock layer ($\epsilon_r = 20$) (Figure 2b).

We then undertake a series of sensitivity experiments with uniform models to investigate the performance of PMLs in attenuating grazing wave energy on the boundary of the sliced-3D model for a sliced-3D model with a fixed domain size of 9 cells and a PML thickness of 15 cells. The experiments are performed at (a) 25 and (b) 50 MHz using a Ricker wavelet. We use a similar approach to Taflove and Hagness (2005) and Drossaert and Giannopoulos (2007) in testing parameter pairs over an expected range to derive the optimum values because, although this is a computationally intensive option, it allows a clear assessment of the sensitivity to different parameters. We initially do this using a κ scaling polynomial $m = 2$ and α polynomial $m = 1$ (see eqs. 7 and 8). The model was discretized at 0.1m to give a model domain size of 24 x 24 x 3.5 m. The PML thickness was extended compared to a typically used 10-cell implementation, with the intention of reducing errors due to normal incidence energy at the bounding edges, which may not be attenuated as effectively when optimisation is undertaken to reduce evanescent energy. We then repeat this approach to investigate the impact of polynomial order m for κ and α, running this test for all combinations between $m = 0$ (constant value) and $m = 6$.

We then investigate the frequency dependence of optimal CFS-PML parameters, by doing a similar grid search parameter test as for the previous tests, but this time using an impulse source type followed by a convolution with a Ricker wavelet with central wavelength λ_c. We limit frequencies used to $20 < \lambda_c/dx < 100$, as this is the most commonly used range of λ/dx for efficient FDTD modelling, also noting the dispersion limit of $dx < \lambda_{min}/10$ (Giannopoulos, 1998) and that for a Gaussian waveform, the minimum significant wavelength considered for dispersion ($error < -40$ dB) is $\lambda_{min} \approx \frac{\lambda_c}{3}$. Using a grid size of 0.01 and 0.1 m this allows testing in the range 100-700 and 10-70 MHz respectively. For this experiment, we use a 5-cell domain width with 15-cell PML.

For each of the above sensitivity experiments a reference solution of a 3D model, $\mathrm{E}(x, y, t)_{\mathrm{ref}}$, is calculated using a large 3D model with an identical 2D geometry, to give the response where there is no interaction with bounding PMLs normal to the z orientation. The 3D model consists of identical geometry in the x- and y-orientation, with a 120-cell model width in the z-orientation and a 10-cell PML using a constant $\kappa_{max} = 1$, and σ scaled linearly between 0 and σ_{max} after equation 6. As a result of this larger width there is no grazing-wave interaction with the model-PML interface, and we can assume this to be the best-case scenario with minimum error response. Errors are reported relative to this reference solution as in Roden and Gedney (2000); Berenger (2002); Giannopoulos (2008);

Taflove and Hagness (2005); Feng et al. (2017) as

$$error(x, y, t) = 20\log_{10}\frac{\mathrm{E}(x, y, t) - \mathrm{E}(x, y, t)_{\mathrm{ref}}}{\mathrm{E}_{\mathrm{ref}_{\mathrm{max}}}}, \tag{11}$$

where $\mathrm{E}(x, y, t)$ is the output electric field in time, $\mathrm{E}(x, y, t)_{\mathrm{ref}}$ is the reference solution in time, and $\mathrm{E}_{\mathrm{ref}_{\mathrm{max}}}$ is the maximum value of the reference solution.

To demonstrate the performance of the sliced-3D approach, we repeat our experiment of investigating domain width sensitivity to confirm that an improvement in error is observed using an optimised CFS-PML, before comparing the performance of an optimised first order PML with those previously published in the literature, including Feng et al. (2017), which was developed for computational seismology but follows similar theory, along with Gedney and Zhao (2010) and as outlined previously. For this case we use a model discretisation of 0.005 m and free space ($\epsilon_r = 1$).

NUMERICAL RESULTS

Impact of domain size

Figure 2 shows the results of reducing domain size for homogeneous and layered models. Thin models (3 cell) model domain size show significant (> -20dB) noise levels at signal arrival, followed by low-frequency ringing as a result of evanescent energy from the model-PML interface. Figure 3 shows the error for both x- and z- polarisations for the homogeneous ice model. We estimate an error of -40 dB (1%) to be a feasible target to reduce the errors below the signal-to-noise ratio of a typical radargram which, from figure 3, would require a domain width of 60 cells. At small domain sizes, the effect of evanescent energy is significant, whereby low frequency and high amplitude errors are introduced following the direct arrival

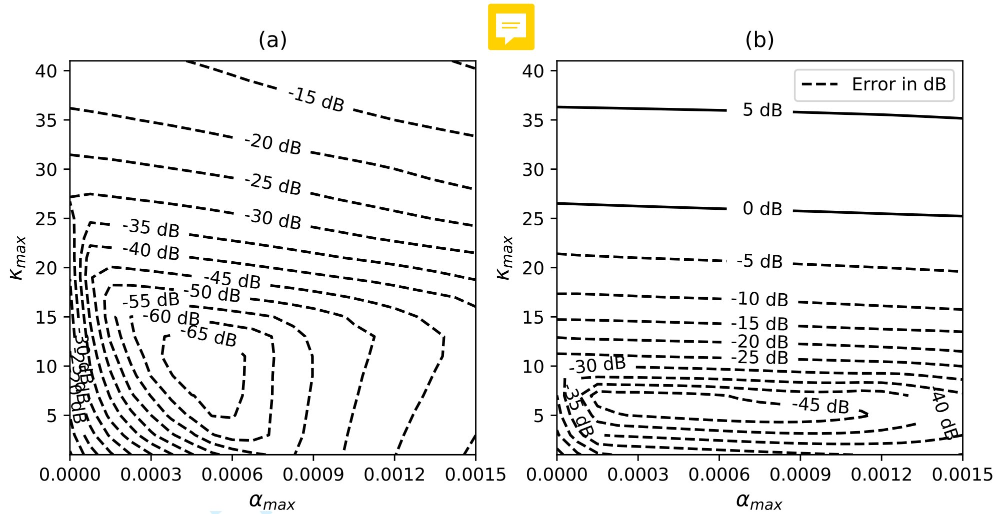

Figure 4: Contour plot of maximum error as a function of α_{max} (frequency shift factor, equation 4) and κ_{max} (stretching factor) for a homogeneous ice model with a 5 cell width model domain, 15 cell first-order PMLs, with $dx = 0.1$m. A Gaussian waveform with central frequency (a) 25 MHz and (b) 50 MHz is used.

(arrivals in Figure 2, marked 'B'). Thickening the PML has minimal impact on this error as it is induced by the model/PML boundary.

1st order PML optimisation

The optimum values for α and κ were estimated through a brute-force grid search approach, producing error contour plots exemplified by Figure 4. The grid search shows minimum error bounds of -65 dB and -45 dB for 25 and 50 MHz, respectively. A clear frequency dependence of the optimum parameters can be seen, indicating that optimum κ_{max} decreases with increasing frequency, and that the sensitivity of error to the α value decreases with increasing frequency. This is intuitive as κ dictates the real coordinate stretch of the PML

- a higher value results in a higher stretch, such that the maximum $\frac{\lambda}{dx}$ within the stretched coordinates of the PML is minimised. The optimum value of α is approximately the same for both experiments, but has a much lower sensitivity in the high frequency.

Impact of Polynomial Order

Figure 5 shows the minimum error for each grid search as a function of order of polynomial scaling. It is clear that, for this example, a constant α scaling function is the most efficient, with a maximum -80 dB error. Higher orders of α result in an error of at least -50 dB. A quadratic κ scaling function is shown to provide the optimum attenuation for all orders of α. This result contrasts with Taflove and Hagness (2005), where it is suggested that $\alpha = 0$ at the outermost grid boundary to enable sufficient travelling wave energy attenuation. Our optimal parameter setting is therefore minimising the effect of evanescent energy, with the remaining noise being primarily as a result of normal-incidence energy at the source point.

Frequency Dependence

Figure 6 shows minimum error, optimum α and optimum κ as a function of $\frac{\lambda}{dx}$, firstly demonstrating (Figure 6 (a)) that error is relatively constant at approximately -70 dB for all values of $\frac{\lambda}{dx}$ tested. Figure 6 (b) shows the optimum selection of κ is linear with $\frac{\lambda}{dx}$, with a linear relationship of

$$\kappa_{max} = 0.14\frac{\lambda}{dx} - 1. \tag{12}$$

In Figure 6 (c), α_{max} is plotted as $\log_{10}\alpha_{max}dx$ as a function of $\frac{\lambda}{dx}$. A negative linear relationship can be plotted for the range $20 < \frac{\lambda}{dx} < 70$, of form $y = mx + c$,

$$log_{10}(dx\alpha) = -0.005\frac{\lambda}{dx} - 4, \tag{13}$$

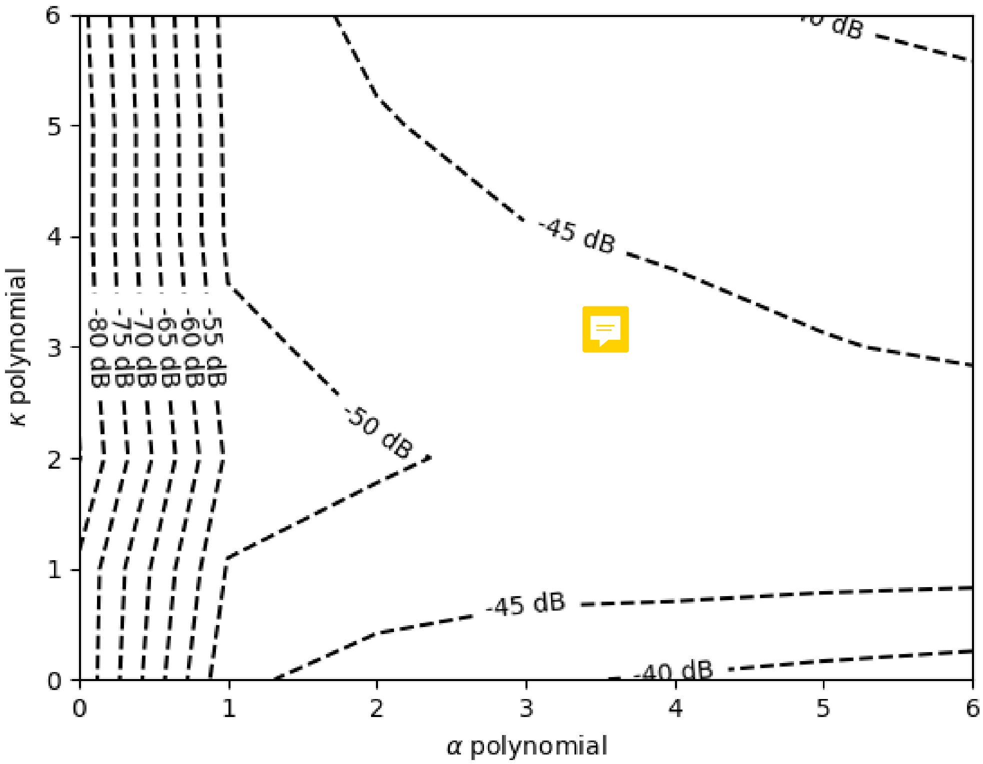

Figure 5: Minimum error for all combinations of polynomial scaling. This is found through repeating the results of Figure 4 for each combination of polynomials in α and κ. The optimum value is shown to be 0 for α and 2 for κ.

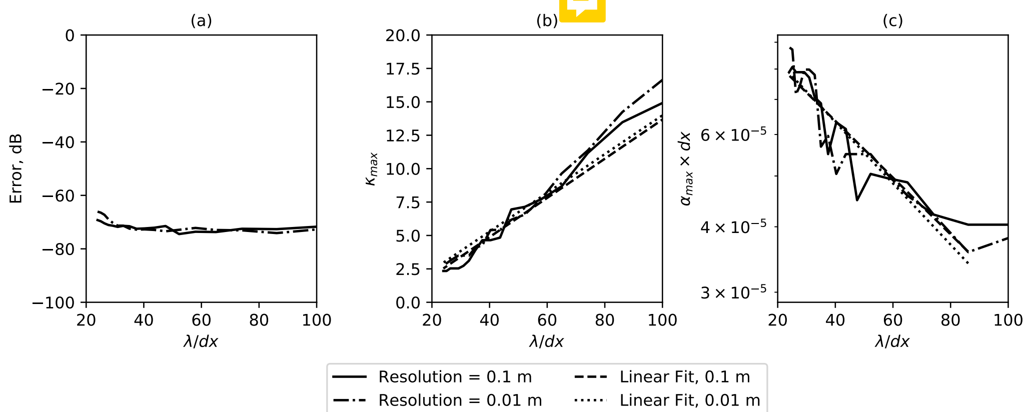

Figure 6: Frequency dependence of the 1st order CFS-PML parameters using a discretisation of 0.1 m and 0.01 m for the homogeneous model (Figure 2a). (a) shows the error as a result of the optimum parameters. (b) shows optimum κ_{max} as a function of $\frac{\lambda}{dx}$. A positive linear trend is observed as expected as a larger κ_{max} is expected for larger wavelengths. (c) shows $\alpha \times dx$ plotted as a function of $\frac{\lambda}{dx}$. This plot is scaled by discretisation on a lin-log plot, demonstrating that optimum α shows a slight negative trend with λ/dx and a scaling with resolution

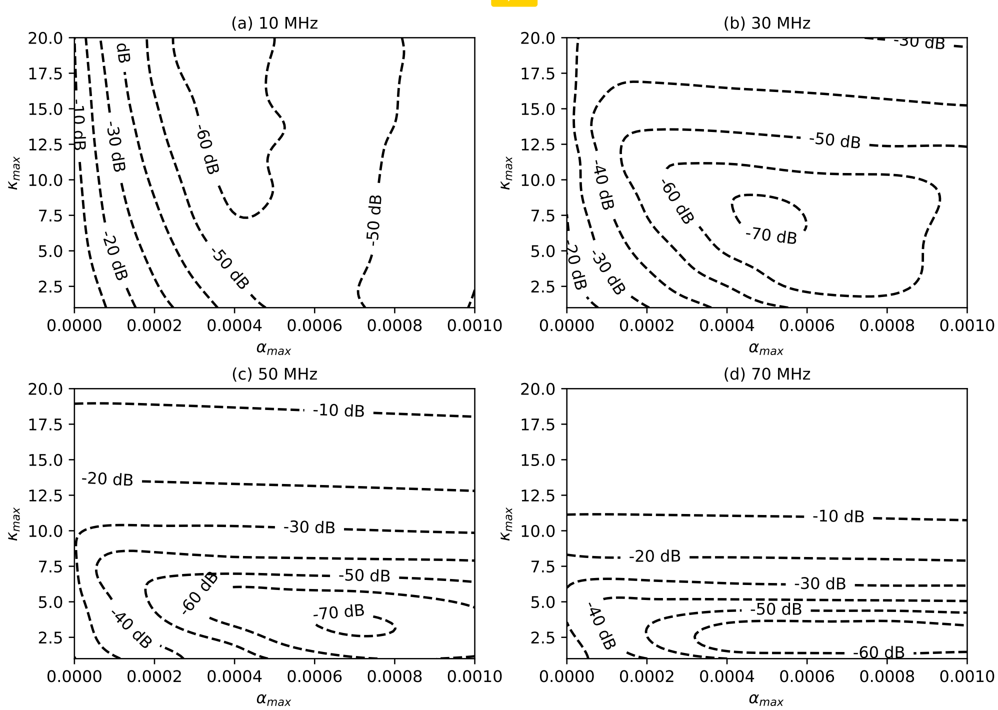

Figure 7: The error surface as a function of κ and α for a range of frequencies for dx=0.01 using the same experimental setup as in Figure 6 (a).

which reduces to

$$\alpha = \frac{10^{-4-0.005\frac{\lambda}{dx}}}{dx}. \tag{14}$$

Together with equation 6, these values can be readily used as a guideline for 1st order CFS-PML parameters in the frequency range suggested as they only require calculation of a central wavelength λ and the discretisation. As such, they can be readily calculated in the FDTD implementation. Figure 7 additionally shows that at higher frequencies (i.e. lower values of λ/dx), the error is much more sensitive to the value of κ_{max} than to the value of α_{max}, and this provides a more stable linear regression result in Figure 6.

Domain width revisited

With our new understanding of optimum CFS-PML parameters, we now revisit signal error as a function of domain width (Figure 8). The optimised PML gives a consistent result of -38 dB for an x-polarised source type, and -45 dB for a z-polarised source type. The error increases slightly at a domain width of 10 cells for a z-polarised source, but remains under -40 dB down to a 3-cell domain width. In the following examples, we use a 5-cell domain width as a balance between computational requirements and accuracy.

Comparison of implementations

The performance of differing implementations is compared in Figure 9 using a sliced-3D homogeneous ice model as in Figure 2 (a), now using 60 receivers in the positive x direction, representing a common source point experiment. The difference between each result and the reference solution in Figure 9 (a) is shown in panels (b) to (e). This demonstrates that a correctly optimised 1st-order CFS-PML can produce synthetic data with no evanescent

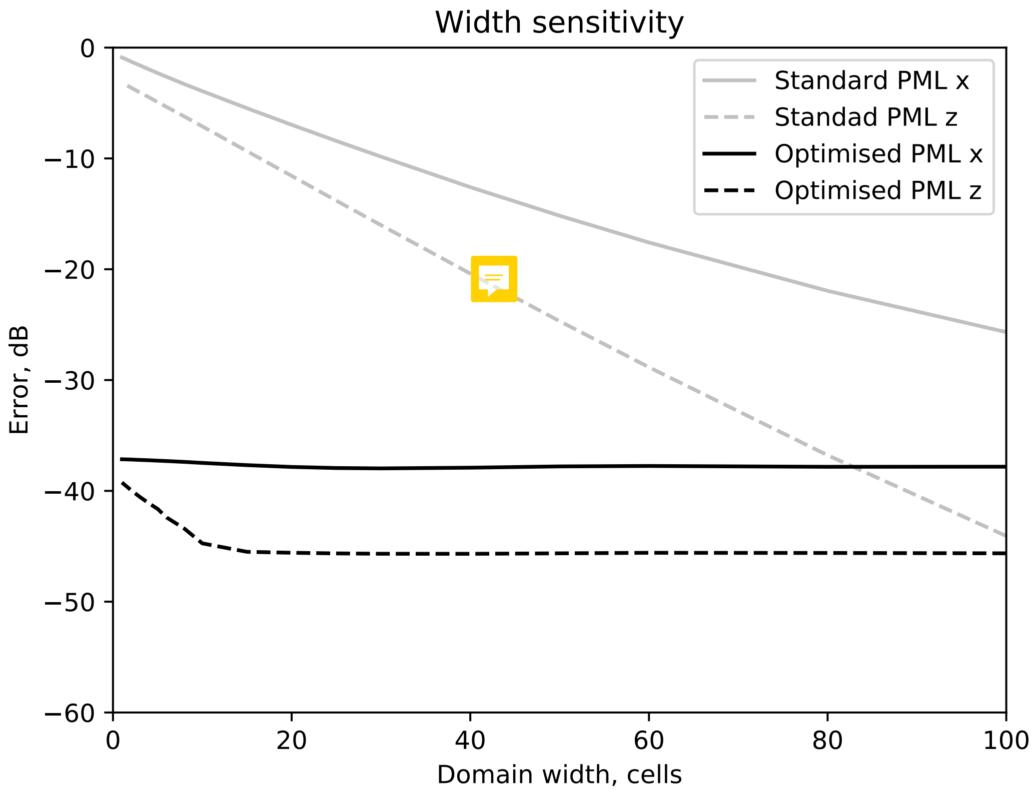

Figure 8: Comparison of the signal error as a function of domain width, as in Figure 3, but including results with an optimised CFS-PML, using the horizontally layered model as in Figure 2c) and d). A consistent -38 dB can be achieved for the x-polarised result and -45 dB for the z-polarisation using our recommendations for CFS PML parameters.

energy in a sliced-3D model domain. There is a slight error close to the source point in ~~panel (c),~~ as a result of the CFS-PML's reduced ability to attenuate normal-incidence energy. Other recommendations (panels (d) and (e)) for CFS-PML parameters show strong evanescent energy, showing that while these have been recommended for a general case for 1st-~~order~~ and 2nd-order CFS-PMLs, they are not suitable in this application.

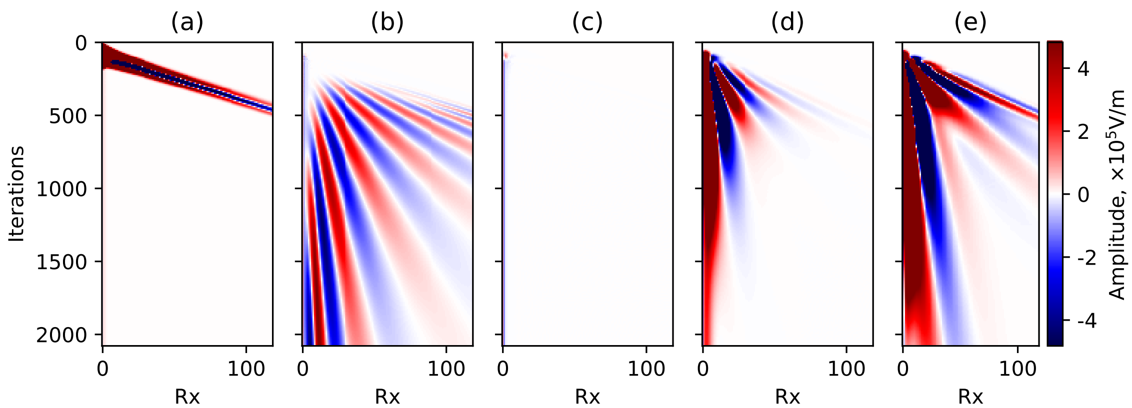

Figure 9: Error plots as a function of receiver offset and time for a 5-cell width sliced 3D domain with a z-polarised source at 50 MHz. Error is the difference between the result and a reference 3D solution. Colour scale is clipped at 1% of the maximum. (a) Reference solution from a 3D model showing direct arrival (b) a sliced-3D domain with no PML parameter optimisation (c) the same model with optimum parameters selected from equations 12 and 14, (d) with parameters selected from the results of Feng et al. (2017) and (e) with parameters recommended by Gedney and Zhao (2010). This comparison demonstrates that a well-optimised 1st order CFS-PML, using recommendations from this study, can show an improvement for grazing-wave interactions over generic parameters chosen for both 1st and 2nd order PMLs, which are often developed for different applications.

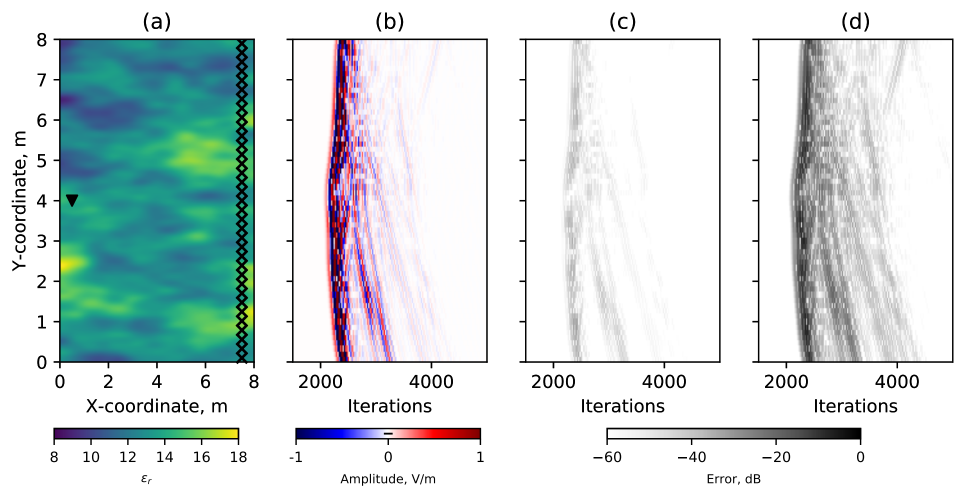

Figure 10: Cross-borehole GPR experiment example. (a) Model domain showing random variations in dielectric constant, overlaid with source point (triangle) and receiver locations (crosses). (b) Results of a full 3D modelling experiment using a z-polarised source. (c) Error plot (in dB) using a sliced-3D domain with parameters recommended in this paper. (d) Error plot (in dB) of 3D-to-2D transformed data using a Bleistein filter

EXAMPLES

Cross-borehole example

We now demonstrate the performance of sliced-3D FDTD modelling in two applications for which error levels and model computational demand are important considerations. We first use a cross-borehole survey configuration in the presence of a heterogeneous soil with ϵ_r ranging between 8 and 18. This is similar to the cross-borehole FWI experiment configurations of Klotzsche et al. (2010) and the computational configuration of Mozaffari et al. (2016). We use a single z-polarised source point with a 200 MHz ~~central frequency~~ Ricker

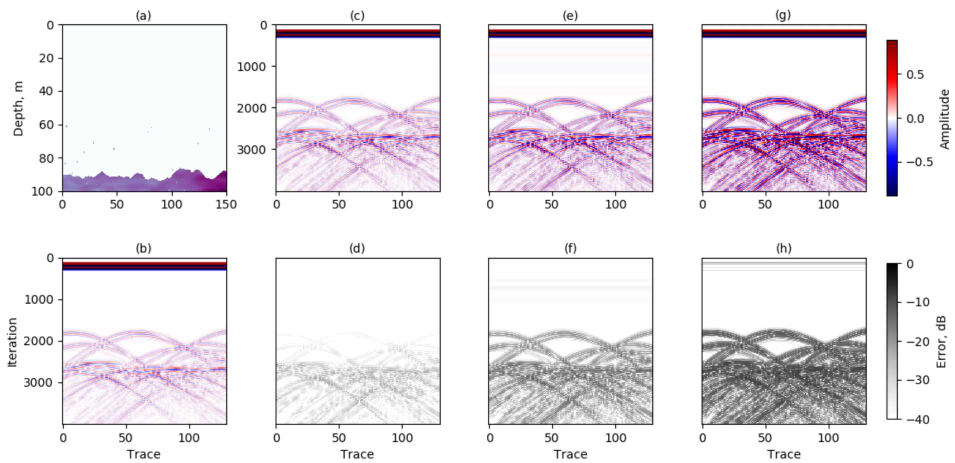

Figure 11: Synthetic representing a glacier bed with internal scattering points within the ice. (a) Initial model with homogeneous ice and a rough bed. (b) Reference model response from full 3D simulation. (c) Model response and (d) error with a sliced-3d domain and an optimised CFS-PML, using the recommendations from section . (e) Model response and (f) error for a sliced-3d domain with no optimised CFS-PML, using $\alpha_{max} = 0$, $\kappa_{max} = 1$ and $\sigma_{max} = \sigma_{opt}$. (g) Model response and (h) error for a 2D model followed by 2D-to-3D Bleistein filter transformation. A significant improvement in error can be observed when the correct source polarisation is used in a sliced-3D approach.

wavelet, with an array of receivers located in a second borehole (see Figure 10a). The source and receiver boreholes are separated by 6 m. Using a discretisation of 0.02 m, the recommended parameters from equations 12 and 14 are $\alpha = 0.00397$ and $\kappa_{max} = 1.80$. We undertake the simulations in 3D, sliced-3D and in 2D. The sliced-3D model domain consisted of 1 cell width, with PMLs extended to 15 cells to minimise noise from normal-incidence energy.

All simulations are undertaken with a z-polarised source to enable like-for-like polarisation comparison with the 2D implementation. We apply a frequency-domain Bleistein 2D-to-3D filter to the 2D data (equation 1), with r equal to the straight line raypath between source and receiver for each trace and c calculated from the RMS value of ϵ_r from the model. We compare the results in figure 10 (c) and (d), which shows a significantly lower error field for the sliced-3D approach.

Common-offset glacier survey example

We now apply this approach to a model of a simple glacier with a rough bed and several internal scattering points. We use model dimensions of 150 x 100 x 3.5 m with a 15 cell PML thickness and resolution 0.1 m to demonstrate the low noise level achievable with our recommendations. A dipole source with a Ricker wavelet ~~of central frequency of 25 MHz~~ is used. Given these model parameters, CFS-PML parameters are chosen to be $\alpha = 0.00046$ and $\kappa_{max} = 3.70$, following Figure 6 and equations 12 and 14. We use a single-channel, common offset survey acquisition with source and receiver separated by 5 m to represent a typical survey with low-frequency dipole antennas. Several scattering points with $\epsilon_r = 80$ are imposed to simulate scattering bodies found within polythermal ice (Barrett et al., 2008). We use 130 source/receiver locations along the surface of a freespace/ice interface.

The results of the model are presented in Figure 11, along with error in dB in the second row ~~(d), (f) and (h).~~ Figure 11 (c) shows the solution for a sliced-3D model with optimised CFS-PML parameters with error compared to a 3D reference. This shows that optimisation of PML parameters can lower the error for scattering bodies to be consistently below -40 dB, with only some later arrivals close to the bed with an error greater -40 dB. Figure 11 (e) shows the response and (f) the error for a sliced-3D model with no PML optimisation. Low-frequency noise is prevalent throughout and errors at the bed are significant. (g) and (h) show the response for a 2D model with 2D-to-3D transformation with the Bleistein filter assuming a first break time of $1\mu s$ for the bed return (2600 iterations Figure 11), and fails to replicate well the amplitudes for any of the scattering or bed returns

DISCUSSION

The numerical results from the examples above show that the errors caused by near-grazing wave interactions with a bounding PML region can be significantly attenuated through optimisation of the first order CFS-PML parameters. We have suggested relationships between optimal parameters and model parameters to attenuate such low-frequency energy significantly as a function of λ/dx, which can be readily calculated using model parameters and source frequency used.

In practice, the effect of κ in the CFS-PML formulation is a real stretching of the cells within the PML region. Higher values of κ result in increasing cell size within the PML region. As such, κ_{max} is a balance between larger stretch and non-attenuated dispersive effects. For larger stretch coefficients, low frequency energy is more effectively attenuated, although large cell sizes can result in numerical dispersion at the outermost bounds of the PML introducing high frequency noise that the PML is not effective at attenuating.

While there have been significant developments in PML implementations through increasingly complex and higher order stretching functions, this study represents the first numerically-based approach to optimise 1st order CFS-PML parameters for a broad range of low frequency geophysical applications. We have compared our results to values published in the literature (Figure 9), although it must be noted that the previous values have been derived and estimated for different applications, and as such the performance cannot always be expected to match those derived for this application.

We have suggested that our parameter choices can be applied for radioglaciological survey, but the effects of a wider range of dielectric materials have not been explored. Regions of higher ϵ_r result in increased numerical dispersion in the propagation, resulting in the requirement of a higher resolution model. In such a case, we require improved attenuation of lower $\frac{\lambda}{dx}$ values, shown in Figure 6 to result in a higher sensitivity of error on κ_{max}. This may be a limitation of the technique in applications to wider geoscientific applications of sliced-3D FDTD modelling.

Further work in this area could explore the improvements that may be attained through optimisation of higher order CFS-PMLs, or through optimisation of recently developed multi-pole PML (Giannopoulos, 2018) However such approaches will necessarily be more complex due to the higher degrees of freedom implicit in these approaches.

CONCLUSIONS

We have shown through numerical modelling that optimisation of a 1st order CFS-PML can be undertaken to minimise domain size to obtain full 3D polarisation synthetics in the case of strictly 2D geometries. Such an approach is required to reduce the impact of grazing-angle evanescent energy close to the model and PML boundary. For a 5-cell domain size with a 15 cell PML, we can reach a maximum amplitude error of -70 dB (or 0.03%) over the typical range of $\frac{\lambda_c}{dx}$ used for efficient numerical modelling. We have suggested relationships between CFS-PML parameters α, κ and $\frac{\lambda}{dx}$ which demonstrate the suitability of such an approach for wider applications of GPR FDTD modelling where consideration of waveform polarisation is important. These recommendations mean this approach is readily applicable in iterative processing algorithms, as parameters can be automatically estimated using the defined model.

REFERENCES

Auer, L., A. M. Nuber, S. A. Greenhalgh, H. Maurer, and S. Marelli, 2013, A critical appraisal of asymptotic 3D-to-2D data transformation in full-waveform seismic crosshole tomography: GEOPHYSICS, **78**, R235–R247.

Barrett, B. E., T. Murray, R. Clark, and K. Matsuoka, 2008, Distribution and character of water in a surge-type glacier revealed by multifrequency and multipolarization ground-penetrating radar: Journal of Geophysical Research, **113**, F04011.

Berenger, J.-P., 2002, Application of the CFS PML to the absorption of evanescent waves in waveguides: IEEE Microwave and Wireless Components Letters, **12**, 218–220.

Bingham, R. G., D. G. Vaughan, E. C. King, D. Davies, S. L. Cornford, A. M. Smith, R. J. Arthern, A. M. Brisbourne, J. De Rydt, A. G. Graham, et al., 2017, Diverse landscapes beneath pine island glacier influence ice flow: Nature communications, **8**, 1–9.

Bleistein, N., 1986, Two-and-one-half dimensional in-plane wave propagation: Geophysical Prospecting, **34**, 686–703.

Busch, S., J. van der Kruk, J. Bikowski, and H. Vereecken, 2012, Quantitative conductivity and permittivity estimation using full-waveform inversion of on-ground GPR data: Geophysics, **77**, H79–H91.

Church, G. J., A. Bauder, M. Grab, S. Hellmann, and H. Maurer, 2018, High-resolution helicopter-borne ground penetrating radar survey to determine glacier base topography and the outlook of a proglacial lake: 2018 17th International Conference on Ground Penetrating Radar (GPR), IEEE, 1–4.

Deregowski, S. M., and S. M. Brown, 1983, A theory of acoustic diffractors applied to 2-D models: Geophysical Prospecting, **31**, 293–333.

Drossaert, F. H., and A. Giannopoulos, 2007, A nonsplit complex frequency-shifted PML based on recursive integration for FDTD modeling of elastic waves: GEOPHYSICS, **72**, T9–T17.

Esmersoy, C., and M. Oristaglio, 1988, Reverse-time wave-field extrapolation, imaging, and inversion: GEOPHYSICS, **53**, 920–931.

Feng, H., W. Zhang, J. Zhang, and X. Chen, 2017, Importance of double-pole CFS-PML for broadband seismic wave simulation and optimal parameters selection: Geophysical Journal International.

Fisher, E., G. A. McMechan, A. P. Annan, and S. W. Cosway, 1992, Examples of reverse-time migration of single-channel, ground-penetrating radar profiles: GEOPHYSICS, **57**, 577–586.

Gedney, S., 1996, An anisotropic perfectly matched layer-absorbing medium for the truncation of FDTD lattices: IEEE Transactions on Antennas and Propagation, **44**, 1630–1639.

Gedney, S. D., and B. Zhao, 2010, An Auxiliary Differential Equation Formulation for the Complex-Frequency Shifted PML: IEEE Transactions on Antennas and Propagation, **58**, 838–847.

Giannopoulos, A., 1998, The investigation of transmission-line matrix and finite-difference time-domain methods for the forward problem of ground probing radar.: PhD thesis, University of York.

———, 2008, An Improved New Implementation of Complex Frequency Shifted PML for the FDTD Method: IEEE Transactions on Antennas and Propagation, **56**, 2995–3000.

———, 2012, Unsplit Implementation of Higher Order PMLs: IEEE Transactions on Antennas and Propagation, **60**, 1479–1485.

———, 2018, Multipole Perfectly Matched Layer for Finite-Difference Time-Domain Electromagnetic Modeling: IEEE Transactions on Antennas and Propagation, **66**, 2987–2995.

King, E. C., H. D. Pritchard, and A. M. Smith, 2016, Subglacial landforms beneath Rutford Ice Stream, Antarctica: detailed bed topography from ice-penetrating radar: Earth Syst. Sci. Data, **8**, 151–158.

Klotzsche, A., L. Lärm, J. Vanderborght, G. Cai, S. Morandage, M. Zörner, H. Vereecken, and J. van der Kruk, 2019, Monitoring soil water content using time-lapse horizontal borehole gpr data at the field-plot scale: Vadose Zone Journal, **18**.

Klotzsche, A., J. van der Kruk, G. Angelo Meles, J. Doetsch, H. Maurer, and N. Linde, 2010, Full-waveform inversion of cross-hole ground-penetrating radar data to characterize a gravel aquifer close to the Thur River, Switzerland: Near Surface Geophysics, **8**, 635–649.

Langhammer, L., L. Rabenstein, A. Bauder, and H. Maurer, 2017, Ground-penetrating radar antenna orientation effects on temperate mountain glaciers: GEOPHYSICS, **82**, H15–H24.

Leuschen, C., and R. Plumb, 2001, A matched-filter-based reverse-time migration algorithm for ground-penetrating radar data: IEEE Transactions on Geoscience and Remote Sensing, **39**, 929–936.

Lomas, A., and A. Curtis, 2019, An introduction to Marchenko methods for imaging: GEOPHYSICS, **84**, F35–F45.

Moghaddam, M., E. J. Yannakakis, and W. C. Chew, 1991, Modeling of the subsurface interface radar: Journal of Electromagnetic Waves and Applications, **5**, 17–39.

Mozaffari, A., A. Klotzsche, G. He, H. Vereecken, J. van der Kruk, C. Warren, and A. Giannopoulos, 2016, Towards 3D full-waveform inversion of crosshole GPR data: 2016 16th International Conference on Ground Penetrating Radar (GPR), IEEE, 1–4.

Roden, J. A., and S. D. Gedney, 2000, Convolution PML (CPML): An efficient FDTD implementation of the CFS-PML for arbitrary media: Microwave and Optical Technology Letters, **27**, 334–339.

Scott, J. B., A. M. Smith, R. G. Bingham, and D. G. Vaughan, 2010, Crevasses triggered on Pine Island Glacier, West Antarctica, by drilling through an exceptional melt layer: Annals of Glaciology, **51**, 65–70.

Sevestre, H., D. I. Benn, N. R. J. Hulton, and K. Baelum, 2015, Thermal structure of Svalbard glaciers and implications for thermal switch models of glacier surging: Journal of Geophysical Research: Earth Surface, **120**, 2220–2236.

Stoyer, C. H., and R. J. Greenfield, 1976, Numerical solutions of the response of a two-dimensional earth to an oscillatory magnetic dipole source: GEOPHYSICS, **41**, 519–530.

Taflove, A., and S. C. Hagness, 2005, Computational electrodynamics : the finite-difference time-domain method: Artech House.

Van Vorst, D. G., M. J. Yedlin, J. Virieux, and E. S. Krebes, 2014, Three-dimensional to two-dimensional data conversion for electromagnetic wave propagation using an acoustic transfer function: application to cross-hole GPR data: Geophysical Journal International Geophys. J. Int, **198**, 474–483.

Versteeg, R. J., 1993, Sensitivity of prestack depth migration to the velocity model: GEOPHYSICS, **58**, 873–882.

Vidale, J., D. V. Helmberger, and R. W. Clayton, 1985, Finite-Difference seismograms for SH waves: Bulletin of the Seismological Society of America, **75**, 1765–1782.

Virieux, J., and S. Operto, 2009, An overview of full-waveform inversion in exploration geophysics: Geophysics, **74**, WCC1–WCC26.

Warren, C., A. Giannopoulos, and I. Giannakis, 2016, gprMax: Open source software to simulate electromagnetic wave propagation for Ground Penetrating Radar: Computer

Physics Communications, **209**, 163–170.

Xu, T., and G. A. McMechan, 1997, GPR attenuation and its numerical simulation in 2.5 dimensions: GEOPHYSICS, **62**, 403–414.

Yang, X., A. Klotzsche, G. Meles, H. Vereecken, and J. Van Der Kruk, 2013, Improvements in crosshole GPR full-waveform inversion and application on data measured at the Boise Hydrogeophysics Research Site: Journal of Applied Geophysics, **99**, 114–124.

Yee, K., 1966, Numerical solution of initial boundary value problems involving maxwell's equations in isotropic media: IEEE Transactions on Antennas and Propagation, **14**, 302–307.

Yilmaz, Ö., 2001, Seismic Data Analysis: Society of Exploration Geophysicists.